Available online at www.sciencedirect.com
ScienceDirect
Journal of the Mechanics and Physics of Solids
55 (2007) 2027–2054

JOURNAL OF THE MECHANICS AND PHYSICS OF SOLIDS

www.elsevier.com/locate/jmps

Computing image stress in an elastic cylinder

Christopher R. Weinberger*, Wei Cai

Department of Mechanical Engineering, Stanford University, CA 94305-4040, USA

Received 12 December 2006; received in revised form 13 March 2007; accepted 17 March 2007

Abstract

We develop numerical methods that efficiently compute image stress fields of defects in an elastic cylinder. These methods facilitate dislocation dynamics simulations of the plastic deformation of micro-pillars. Analytic expressions of the image stress have been found in the Fourier space, taking advantage of the translational and rotational symmetries of the cylinder. To facilitate numerical calculation, the solution is then transformed into the stress field in an infinite elastic body produced by a distribution of body forces or image dislocations. The use of the fast Fourier transform (FFT) method makes the algorithms numerically efficient.

Keywords: Dislocations; Crystal plasticity

1. Introduction

Reliable fabrication and functioning of novel devices at the micro and nano scales requires an understanding of the strength of crystals at these scales. While dislocation motion in crystals (Hirth and Lothe, 1982) is known as the fundamental mechanism of plastic deformation under a wide range of conditions, a quantitative connection between the collective dynamics of dislocations and the plastic strength of the crystal is still lacking. For bulk crystals, plastic strength such as flow stress can be measured experimentally and considered as a size-independent material property. However, as the size of the material decreases to micro and nano scales, the measured plastic strength is found to be size-dependent (Swadener et al., 2002; Uchic et al., 2004; Wu et al., 2005; Nicola et al., 2006).

*Corresponding author.
E-mail addresses: cweinber@stanford.edu (C.R. Weinberger), caiwei@stanford.edu (W. Cai).

0022-5096/$ - see front matter
doi:10.1016/j.jmps.2007.03.007

The origin of this size-dependence is generally attributed to the behavior of dislocations in small volumes.

For example, compression of single-crystal micro-pillars (Greer et al., 2005) showed that the flow stress increases dramatically when the pillar diameter drops below 1 μm, exhibiting a size effect in the absence of an imposed strain gradient. To explain this behavior, a dislocation starvation model was proposed (Nix et al., 2004; Greer and Nix, 2006), whereby in smaller samples the dislocations escape to the surface more quickly and plastic deformation relies more on the supply of dislocations nucleated from the surface. Competing models for the fundamental mechanisms also exist. Zuo and Ngan (2006) argued that the volume-dependent rate of dislocation nucleation is sufficient to explain the observed size effect. However, Uchic et al. (2006) reported the existence of dislocation structures in Ni_3Al pillars similar to those in the bulk, indicating the persistence of the conventional Taylor hardening mechanism down to small scales. Therefore, more detailed theoretical modeling and comparison with experiments is needed to identify the true mechanism for the observed size effect.

Dislocation dynamics (DD) simulations have been developed as a way to link the fundamental dislocation physics and the plasticity of bulk crystals (Devincre and Kubin, 1997; Schwarz, 1999; Ghoniem and Sun, 1999) and thin films (Schwarz, 2003; Ghoniem and Han, 2005; Nicola et al., 2006). With the use of massively parallel computers, DD simulations have successfully captured the strain hardening behavior of a $(10\,\mu m)^3$ volume of a bulk crystal (Cai et al., 2004; Bulatov et al., 2004), which is larger than the volume of a typical micro-pillar in the experiments. This means that we can potentially model the behavior of *all* dislocations in the micro-pillar during the compression test, which presents a unique opportunity to connect theoretical models with experiments. In order to do so, we need to faithfully account for the effect of the cylindrical surface on the dislocations. An important effect is the image stress that attracts the dislocations toward the surface. In this paper, we present efficient methods to compute the image stress for DD simulations of the plastic deformation of a cylinder.

2. Image stress problem

In DD simulations, the dislocations are usually discretized into straight segments connecting a set of nodes (Weygand et al., 2001; Cai et al., 2004). The most time-consuming part of a DD simulation is the evaluation of the forces on the nodes, which are proportional to the stress field integrated on the neighboring segments with appropriate weighting functions. The stress field is the sum of the external stress, usually a constant, and the internal stress due to the dislocation segments themselves, which varies from point to point. The internal stress field of an arbitrary dislocation segment has analytic expressions for an infinite linear isotropic solid, which is usually a good approximation of a bulk crystal. However, for elastic bodies with large surface to volume ratios, the effects of surfaces need to be accounted for explicitly. Unfortunately, analytic expressions for the internal stress usually do not exist, except for highly idealized situations (Gosling and Willis, 1994).

To obtain the internal stress field of a dislocation in an elastic medium Ω with free surface S, we usually need to solve the image stress problem, which is originally introduced by Eshelby (1979). Let σ_{ij}^{∞} be the internal stress field of the same dislocation in an infinite

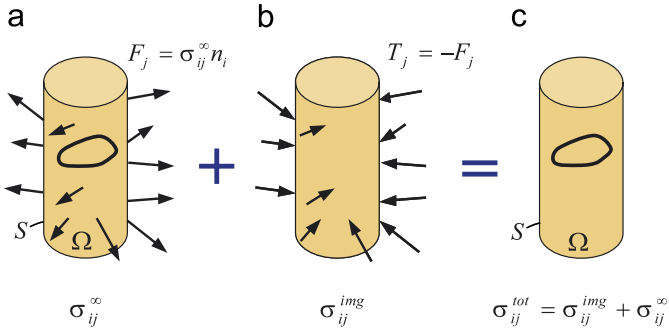

Fig. 1. (a) The internal stress field, σ^{∞}_{ij}, of a dislocation loop in an infinite body requires surface tractions F_j when applied to a finite body. (b) The image stress field σ^{img}_{ij} is the response of a defect-free finite body to surface tractions $T_j = -F_j$. (c) The total internal stress field of a finite body with zero surface tractions is $\sigma^{\text{tot}}_{ij} = \sigma^{\infty}_{ij} + \sigma^{\text{img}}_{ij}$.

body. When applied to domain Ω, it requires a set of tractions on surface S

$$F_j = \sigma^{\infty}_{ij} n_i \tag{1}$$

in order to satisfy equilibrium, as shown in Fig. 1(a). If the domain Ω is subjected to zero-traction (i.e. free surface) boundary conditions, we need an image solution which cancels T_j on the surface when superimposed on the infinite body solution. We denote the image stress σ^{img}_{ij}, which is the stress in a dislocation-free medium Ω when its surface S is subjected to tractions

$$T_j = -F_j = -\sigma^{\infty}_{ij} n_i. \tag{2}$$

The total internal stress in Ω under zero surface traction is then

$$\sigma^{\text{tot}}_{ij} = \sigma^{\text{img}}_{ij} + \sigma^{\infty}_{ij}. \tag{3}$$

Therefore, the forces on the dislocation nodes inside Ω contain contributions from the infinite-body stress σ^{∞}_{ij}, the image stress σ^{img}_{ij}, and the external stress, integrated on the neighboring segments.

The superposition approach outlined above can be generalized by considering the dislocation stress field $\sigma^{\tilde{\Omega}}_{ij}$ in an arbitrary domain $\tilde{\Omega}$ must contain the domain of interest, (i.e. $\Omega \subset \tilde{\Omega}$) but does not have to be infinite. As long as the analytic solution of the stress field $\sigma^{\tilde{\Omega}}_{ij}$ exists, it can be used to construct the stress field of interest, $\sigma^{\text{tot}}_{ij} = \sigma^{\tilde{\Omega}}_{ij} + \sigma^{\text{img}}_{ij}$. In this case, the image stress field, σ^{img}_{ij}, is defined as the stress induced in domain Ω when its surface S is subjected to traction $T_j = -\sigma^{\tilde{\Omega}}_{ij} n_i$. In most part of this paper, we will consider $\tilde{\Omega}$ as the infinite medium. However, in some cases it may be advantageous to consider $\tilde{\Omega}$ as an elastic half space whose flat surface is tangent to the cylinder. An analytic solution exists for the dislocation stress field in an isotropic elastic half space (Gosling and Willis, 1994). More discussion along this line is given in Section 4.1.

To evaluate the total forces on dislocations inside Ω, we need to compute the stress field produced in Ω in response to a general set of surface tractions. The standard method to do so is the finite element method (FEM), which has been combined with DD methods to solve the image stress (Weygand et al., 2001, 2002). However, it is of interest to develop more efficient methods, because DD simulations require a lot of image stress calculations

to high accuracy. For example, DD simulations of crystal plasticity usually requires $\sim 10^6$ time steps and the image stress field needs to be computed at each step. Furthermore, the stress field must be integrated over line segments to compute nodal forces. This increases the computational load if the integration is done numerically. This paper presents four alternative image stress methods which are potentially more efficient.

3. Analytic solutions of image stress in a cylinder

An important advantage of FEM is that, being a general method, it is applicable to elastic bodies with arbitrary shapes. However, for elastic bodies with special shapes, we may be able to take advantage of the symmetries and develop analytic tools that can lead to more efficient and accurate methods. If we assume periodic boundary conditions (PBC) along its axis, an elastically isotropic cylinder has translational symmetry along and rotational symmetry around this axis. An arbitrary surface traction can be decomposed into a sum of Fourier modes (plane waves) on the cylinder surface. Because of the symmetries, these Fourier modes do not couple with each other. The stress field produced by each Fourier mode can be obtained analytically and the image stress field is the summation of the contributions from all Fourier modes. This is the basic idea behind the methods to be presented below. Section 3.1 gives an overview of the four different methods to be discussed in detail. Section 3.2 describes the analytic solutions of an elastic cylinder subjected to a plane-wave surface traction, which leads to Method I. Section 3.3 describes a similar set of solutions for an inverted cylinder, i.e. an infinite medium with a cylindrical hole, subjected to a plane-wave traction on its internal surface. Section 3.4 combines these two solutions together and maps the original cylinder problem to an infinite body with different internal stress sources. These mappings lead to Methods II–IV of image stress calculation, which will be discussed in Section 3.5. Numerical benchmark results of these methods will be compared in Section 4. The numerical efficiency scaling behavior of these methods in comparison with conventional FEM and boundary element methods (BEMs) will be discussed in Section 5.

3.1. Solution overview

Consider an elastically isotropic cylinder with length L subjected to PBC along its axis shown in Fig. 3. Let $\mathbf{T}(z,\theta)$ be an arbitrary distribution of traction forces on the cylindrical surface, which can be represented in terms of Fourier modes

$$\mathbf{T}(z,\theta) = \sum_k \sum_n \hat{\mathbf{T}}(k_z, n) \exp[\mathrm{i}k_z z + \mathrm{i}n\theta], \tag{4}$$

where $k_z = 2\pi k/L$ and k, n are integers. For each Fourier mode, the displacement field inside the cylinder, $\hat{\mathbf{u}}(k_z, n, r)$, can be found analytically (see Section 3.2), so that the displacement field in response to the traction force can be found simply by superposition,

$$\mathbf{u}(z,\theta,r) = \sum_k \sum_n \hat{\mathbf{u}}(k_z, n, r) \exp[\mathrm{i}k_z z + \mathrm{i}n\theta]. \tag{5}$$

The stress field follows from the displacement field simply by taking a spatial derivative and multiplying the elastic constants.

$$\boldsymbol{\sigma}(z,\theta,r) = \sum_k \sum_n \hat{\boldsymbol{\sigma}}(k_z, n, r) \exp[\mathrm{i}k_z z + \mathrm{i}n\theta]. \tag{6}$$

In practice, the traction force distribution $\mathbf{T}(z,\theta)$ can be sampled on a $n_q \times n_z$ regular mesh on the cylindrical surface, where n_q and n_z are the number of sampling points along the perimeter and length of the cylinder, respectively. The traction forces are best represented in cylindrical coordinates, i.e. $\mathbf{T} = (T_r, T_\theta, T_z)$, leading to three $n_q \times n_z$ matrices. The Fourier coefficients, $\hat{\mathbf{T}} = (\hat{T}_r, \hat{T}_\theta, \hat{T}_z)$, can then be obtained by 2-dimensional fast Fourier transforms (FFT) of the three matrices, T_r, T_θ and T_z, separately. Given these Fourier coefficients, the stress field at an arbitrary point inside the cylinder can be obtained analytically from Eq. (6) by summing over $n_q \times n_z$ Fourier modes. Because the summation over Fourier modes is truncated, the stress field obtained in this way will be more accurate with increasing n_q and n_z. The analytic expressions for $\hat{\mathbf{u}}(k_z, n, r)$ and $\hat{\boldsymbol{\sigma}}(k_z, n, r)$ involve Bessel functions of r, thus we will refer to this method of computing the image stress as Method I (*Bessel*).

We can improve the numerical efficiency of Method I and simplify its implementation by transforming the original problem of an elastic cylinder into that of an infinite elastic medium. The two problems are equivalent in the sense that the stress field inside the cylindrical region of the infinite body exactly matches the stress field inside the original cylinder. In order to satisfy this condition, the infinite medium needs to contain a set of internal stress sources on its internal cylindrical interface, either in the form of body forces, $\mathbf{f}(z,\theta)$, displacement discontinuities $[|\mathbf{u}|](z,\theta)$, or dislocations $\mathbf{b}(z,\theta)$; they will be called *equivalent stress sources*. Because the stress field generated by body forces, displacement discontinuities, and dislocation lines in an infinite medium involves Green's function, Volterra's formula and Mura's formula, we arrive at three new methods, which will be called: Method II (*Green*), Method III (*Mura*), and Method IV (*Volterra*). The distribution of these equivalent stress sources, e.g. $\mathbf{f}(z,\theta)$ and $[|\mathbf{u}|](z,\theta)$, are first obtained in the Fourier space and then transformed to real space by FFT. Fig. 2 sketches the flow chart of all four methods. Their details will be presented in the following sections. The transformation of the original cylinder problem to an equivalent problem of an infinite body also leads to a simple expression for the elastic energy. This allows us to check the self-consistency between force and energy, as will be verified in Section 4.

3.2. Solution of a cylinder in Fourier space

Analytic solutions of an infinite and elastically isotropic cylinder subjected to arbitrary surface tractions have been proposed at the end of the 19th century by Pochammer (1876) and Chree (1889). Dynamic wave propagation along an infinite elastic cylinder has also been studied (Achenbach, 1982; Kim and Steele, 1989a, b, 1990). Recent work on static problems is focused on finite or semi-infinite length cylinders (see references in Chau and

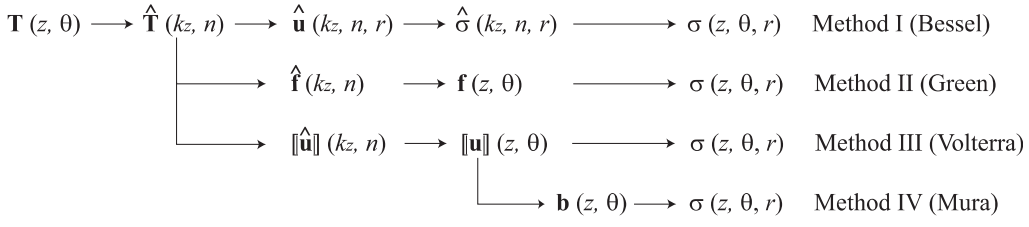

Fig. 2. Flow chart for the four different methods of image stress calculation.

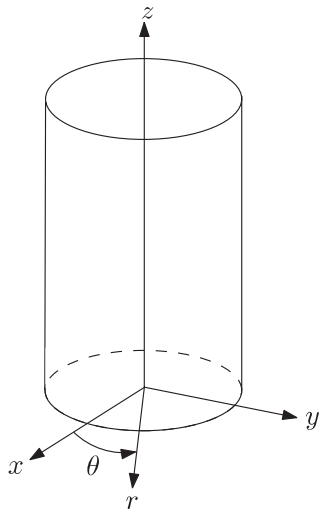

Fig. 3. The Cartesian (x, y, z) and cylindrical (r, θ, z) coordinate systems to describe an elastic cylinder.

Wei, 2000). While most of these analyses are restricted to axisymmetric loading (Kim and Steele, 1992; Wei and Chau, 2000), a solution for finite length cylinders under arbitrary surface load has been proposed (Chau and Wei, 2000). In this work, we make the simplifying assumption that the cylinder is subjected to PBC so that the end effects can be ignored. It is then relatively easy to adapt the dynamic wave solutions obtained earlier to the static problem. While various analytic approaches exist to solve elasticity problems of a cylinder, we will follow the displacement potential approach, similar to that used by Achenbach (1982). The resulting solution is equivalent to that obtained by Pochammer (1876) and Chree (1889), but the use of displacement potential makes the derivation much easier to follow.

The equilibrium condition in an isotropic body can be written in terms of the displacement field, $\mathbf{u}$, as

$$\mu\nabla^2\mathbf{u} + (\lambda + \mu)\nabla\nabla\cdot\mathbf{u} = 0, \tag{7}$$

where λ and μ are Lamé constants. The displacements can be written in terms of displacement potentials, ϕ (scalar potential) and $\boldsymbol{\psi}$ (vector potential), as

$$\mathbf{u} = \boldsymbol{\nabla}\phi + \boldsymbol{\nabla}\times\boldsymbol{\psi} \tag{8}$$

and the equilibrium condition reduces to (Achenbach, 1982)

$$\boldsymbol{\nabla}[(\lambda + 2\mu)\nabla^2\phi] + \boldsymbol{\nabla}\times[\mu\nabla^2\boldsymbol{\psi}] = 0. \tag{9}$$

The general solution of this equation in an infinite elastic cylinder can be expressed as

$$\phi = \frac{\mu}{\lambda + 2\mu}\sum_n\sum_{k_z} A_{(k_z,n)} r\frac{\mathrm{d}}{\mathrm{d}r}J_n(\mathrm{i}k_z r)\,\mathrm{e}^{\mathrm{i}n\theta + \mathrm{i}k_z z}, \tag{10}$$

$$\psi_r = \sum_n \sum_{k_z} \left[\mathrm{i} B_{(k_z,n)} J_{n+1}(\mathrm{i}k_z r) - \mathrm{i} A_{(k_z,n)} r \frac{\mathrm{d}}{\mathrm{d}r} J_{n+1}(\mathrm{i}k_z r) \right] \mathrm{e}^{\mathrm{i}n\theta + \mathrm{i}k_z z}, \tag{11}$$

$$\psi_\theta = \sum_n \sum_{k_z} \left[B_{(k_z,n)} J_{n+1}(\mathrm{i}k_z r) - A_{(k_z,n)} r \frac{\mathrm{d}}{\mathrm{d}r} J_{n+1}(\mathrm{i}k_z r) \right] \mathrm{e}^{\mathrm{i}n\theta + \mathrm{i}k_z z}, \tag{12}$$

$$\psi_z = \sum_n \sum_{k_z} \left[\mathrm{i} C_{(k_z,n)} J_n(\mathrm{i}k_z r) + \mathrm{i} A_{(k_z,n)} r \frac{\mathrm{d}}{\mathrm{d}r} J_n(\mathrm{i}k_z r) \right] \mathrm{e}^{\mathrm{i}n\theta + \mathrm{i}k_z z}. \tag{13}$$

This solution is similar to the dynamic (wave) solution presented in Achenbach (1982) but additional terms (associated with $A_{(k_z,n)}$) are added to remove degeneracy in the static limit. The solution described in Eqs. (10)–(13) is applicable to elastic fields that vary in both the z- and the θ-directions. The solutions that do not vary in the z-direction must be handled separately. These special cases are detailed in Appendix A.

Given the displacement field, the stress field can be obtained by taking spatial derivatives and multiplying the elastic constants. To save space, the explicit expressions for the stress components are not included here, but they do depend on the coordinates r, θ and z, as well as on coefficients $A_{(k_z,n)}$, $B_{(k_z,n)}$ and $C_{(k_z,n)}$, and can be expressed in the following matrix form:

$$\begin{pmatrix} \sigma_{rr} \\ \sigma_{\theta\theta} \\ \sigma_{zz} \\ \sigma_{r\theta} \\ \sigma_{rz} \\ \sigma_{\theta z} \end{pmatrix} = \mathbf{D}(r) \cdot \begin{pmatrix} A \\ B \\ C \end{pmatrix} \mathrm{e}^{\mathrm{i}n\theta + \mathrm{i}k_z z}, \tag{14}$$

where for brevity we have omitted the subscripts (k_z, n) that specifies each Fourier mode. The coefficients A, B and C for each Fourier mode can be determined by matching the boundary conditions at the cylindrical surface, where a specified traction force $\mathbf{T}(z,\theta)$ is applied. The traction force corresponding to Fourier mode (k_z, n) is $\hat{\mathbf{T}}(k_z, n)\,\mathrm{e}^{\mathrm{i}n\theta + \mathrm{i}k_z z}$, as given in Eq. (4). Let $\hat{T}_r$, $\hat{T}_\theta$, $\hat{T}_z$ be the components of $\hat{\mathbf{T}}(k_z, n)$ in cylindrical coordinates. They are identical to σ_{rr}, $\sigma_{r\theta}$, σ_{rz} in Eq. (14), when evaluated at the outer radius $r = 1$. Therefore, $\hat{T}_r$, $\hat{T}_\theta$, $\hat{T}_z$ and A, B, C are related by

$$\begin{pmatrix} \hat{T}_r \\ \hat{T}_\theta \\ \hat{T}_z \end{pmatrix} = \mathbf{M} \cdot \begin{pmatrix} A \\ B \\ C \end{pmatrix}, \tag{15}$$

where matrix $\mathbf{M}$ is a sub-matrix of matrix $\mathbf{D}(r)$ evaluated at $r = 1$. A different matrix $\mathbf{M}$ exists for each Fourier mode (k_z, n). The analytic expression for matrix $\mathbf{M}$ is given in Appendix A.

The coefficients of every Fourier mode can be obtained by the following procedure. The traction force distribution $\mathbf{T}(z,\theta)$ is first sampled on a $n_q \times n_z$ regular mesh on the cylindrical surface and expressed in cylindrical coordinates, $\mathbf{T} = (T_r, T_\theta, T_z)$, leading to three $n_q \times n_z$ matrices. The values of $\hat{T}_r$, $\hat{T}_\theta$, $\hat{T}_z$ for each Fourier mode (k_z, n) is obtained by 2-dimensional FFTs of the T_r, T_θ, T_z matrices, respectively. The coefficients A, B, C are then obtained by solving Eq. (15) through the inverse of matrix $\mathbf{M}$ for each Fourier mode.

In a few special cases, the matrix **M** will be singular, i.e. its inverse does not exist. This corresponds to net applied forces or moments that the cylinder cannot support physically. Fortunately, when we are trying to solve an image stress problem, these unphysical force distributions should not arise in the first place. The numerical procedure to treat these special cases is discussed in Appendix A. This procedure is very efficient with the use of FFT. The inverse of the matrix **M** can be pre-computed, so the solution of Eq. (15) involves at most the multiplication of a 3×3 matrix for each Fourier mode. Once the Fourier coefficients are determined, the stress field at any point inside the cylinder can be obtained by superimposing the contributions, Eq. (14), from every Fourier mode.

Similarly, we can also apply displacement boundary conditions to the cylinder surface. The surface displacement for each Fourier mode (k_z, n) are related to the Fourier coefficients through another matrix **N**,

$$\begin{pmatrix} \overline{u}_r \\ \overline{u}_\theta \\ \overline{u}_z \end{pmatrix} = \mathbf{N} \cdot \begin{pmatrix} A \\ B \\ C \end{pmatrix}, \tag{16}$$

where again we have omitted the subscript (k_z, n) for brevity. Similarly, this expression can be inverted to solve for the coefficients A, B, and C, from a specified displacement field. In this case, the **N** matrices will always be invertible, because the displacement potentials in Eqs. (10)–(13) can represent arbitrary displacement fields. This solution will be used later to map the elastic cylinder problem to an equivalent problem of an infinite elastic medium containing a set of image dislocations.

3.3. Solution of an inverted cylinder in Fourier space

The solution to the inverted cylinder (i.e. an infinite medium containing a cylindrical hole) subjected to arbitrary surface tractions (on the inner surface of the hole) can be found in much the same way as for the cylinder. However, the Bessel functions in Eqs. (10)–(13) must be replaced by functions that satisfy the same set of equations but have a well-defined limit as $r \to \infty$. Thus, for the inverted cylinder problem the general expression for the displacement potential is

$$\phi = \frac{\mu}{\lambda + 2\mu} \sum_n \sum_{k_z} A'_{(k_z,n)} r \frac{\mathrm{d}}{\mathrm{d}r} H_n^{(\alpha)}(\mathrm{i}k_z r) \mathrm{e}^{\mathrm{i}n\theta + \mathrm{i}k_z z}, \tag{17}$$

$$\psi_r = \sum_n \sum_{k_z} \left[\mathrm{i}B'_{(k_z,n)} H_{n+1}^{(\alpha)}(\mathrm{i}k_z r) - \mathrm{i}A'_{(k_z,n)} r \frac{\mathrm{d}}{\mathrm{d}r} H_{n+1}^{(\alpha)}(\mathrm{i}k_z r) \right] \mathrm{e}^{\mathrm{i}n\theta + \mathrm{i}k_z z}, \tag{18}$$

$$\psi_\theta = \sum_n \sum_{k_z} \left[B'_{(k_z,n)} H_{n+1}^{(\alpha)}(\mathrm{i}k_z r) - A'_{(k_z,n)} r \frac{\mathrm{d}}{\mathrm{d}r} H_{n+1}^{(\alpha)}(\mathrm{i}k_z r) \right] \mathrm{e}^{\mathrm{i}n\theta + \mathrm{i}k_z z}, \tag{19}$$

$$\psi_z = \sum_n \sum_{k_z} \left[\mathrm{i}C'_{(k_z,n)} H_n^{(\alpha)}(\mathrm{i}k_z r) + \mathrm{i}A'_{(k_z,n)} r \frac{\mathrm{d}}{\mathrm{d}r} H_n^{(\alpha)}(\mathrm{i}k_z r) \right] \mathrm{e}^{\mathrm{i}n\theta + \mathrm{i}k_z z}, \tag{20}$$

where α equals 1 or 2 and denotes the Hankel functions of the first or second kind. To give the correct limiting behavior of the Hankel functions (with purely imaginary arguments), $\alpha = 1$ when $k_z > 0$ and $\alpha = 2$ when $k_z < 0$. The stress fields can be obtained from the displacement potential in the same way as before. The stress field contribution from each

Fourier mode can be expressed in terms of the yet undetermined coefficients, A', B', and C', in a matrix form

$$\begin{pmatrix} \sigma_{rr} \\ \sigma_{\theta\theta} \\ \sigma_{zz} \\ \sigma_{r\theta} \\ \sigma_{rz} \\ \sigma_{\theta z} \end{pmatrix} = \mathbf{D}'(r) \cdot \begin{pmatrix} A' \\ B' \\ C' \end{pmatrix} e^{in\theta + ik_z z}. \tag{21}$$

The coefficients can be related to the surface tractions prescribed on the hole surface ($r = 1$) through the relationship

$$\begin{pmatrix} \hat{T}_r \\ \hat{T}_\theta \\ \hat{T}_z \end{pmatrix} = \mathbf{M}' \cdot \begin{pmatrix} A' \\ B' \\ C' \end{pmatrix}, \tag{22}$$

where $\mathbf{M}'$ is a sub-matrix of $\mathbf{D}'(r)$ evaluated at $r = 1$. The traction forces on the inner surface of the cylindrical hole are $(-\hat{T}_r, -\hat{T}_\theta, -\hat{T}_z)$ when expressed in cylindrical coordinates. The inverted cylinder problem also has a number of special cases, in some of which $\mathbf{M}'$ cannot be inverted. The analytic expressions for $\mathbf{M}'$ and these special cases are discussed in detail in Appendix B.

Similarly, if the cylindrical surface is subjected to a prescribed displacement boundary condition, the Fourier coefficients can be obtained from their relationship with the surface displacements

$$\begin{pmatrix} \overline{u}_r \\ \overline{u}_\theta \\ \overline{u}_z \end{pmatrix} = \mathbf{N}' \cdot \begin{pmatrix} A' \\ B' \\ C' \end{pmatrix}. \tag{23}$$

Thus, the unknown Fourier coefficients A', B' and C' can be determined by Fourier transforming the applied traction or displacement fields and inverting Eq. (22) or (23). The resulting stress field can then be found by superimposing the contributions, Eq. (21), from every Fourier mode, in exactly the same way as for the cylinder problem.[1]

3.4. Equivalent problems in an infinite medium

In the above we have described an FFT-based method to find the stress field at an arbitrary point in an elastic cylinder subjected to arbitrary traction forces on the boundary. This can be used to compute image stress fields due to the free surface in a DD simulation. However, it is desirable to further improve the numerical efficiency of this method for the following reasons.

[1]The solution for the inverted cylinder is introduced here to facilitate the computation of the image stress of dislocations in a cylinder (Section 3.4). In this context, the inverted cylinder will be subjected to surface tractions but will not contain dislocations. The solution developed here can also be used to compute the image stress for dislocations inside an inverted cylinder (which is beyond the scope of this paper). In this case, the elastic medium is multi-connected medium and the choice of the cut-plane for the dislocation affects the stress field (Lubarda, 1999).

First, the calculation of stress at a given point still requires a summation over all Fourier modes, which is time consuming. Let $N_m = n_q \times n_z$ be the number of grid points on the surface mesh. N_m is also the number of Fourier modes that need to be summed together to compute stress. The most time-consuming part in determining the Fourier coefficients of the solution is the transformation of surface traction into Fourier space. With FFT, this computational time scales as $N_m \log N_m$, which is very efficient. However, after the Fourier coefficients have been determined, the calculation of the image stress on N_s dislocation segments still requires $\mathcal{O}(N_m N_s)$ number of operations, which is inefficient. Suppose if we can convert the stress generated by these N_m Fourier modes into N_m equivalent stress sources (such as a distribution of body forces or image dislocations) in the real space, then more efficient algorithms can be applied to compute the stress field. For example, in the fast multipole method (FMM), only the contributions from stress sources close to the point of interest will be evaluated individually. Contributions from stress sources that are farther away are lumped together and represented by a multipole expansion. This should significantly improve the computational efficiency.

Second, in DD simulations, we need to integrate the stress field along straight dislocation segments. This will significantly raise the computational cost if the integration is performed numerically—by evaluating the stress at multiple points on each segment. It would be useful if we can find analytic expressions for the image stress field integrated over arbitrary straight segments. For the stress field generated by a point force or a straight dislocation segment in an infinite elastic medium, its integral over another straight segment can be obtained analytically. For example, these analytic expressions have been used in DD simulations in the bulk (Cai et al., 2004; Arsenlis et al., 2007) to improve computational efficiency. Converting the cylinder problem to an infinite-medium problem would allow us to take advantage of both FMM and analytic integration.

In this section, we will map the original cylinder problem to an equivalent problem of an infinite medium. The two problems are equivalent in the sense that in a cylindrical region inside the infinite medium the stress field is identical to that in the original cylinder. To satisfy this condition, the infinite medium should contain a set of *equivalent stress sources*, either as body forces or as image dislocations, distributed on its internal cylindrical interface. First, the distribution of these equivalent stress sources needs to be solved for. After that, the stress field produced by these sources can be computed based on analytic expressions.

The procedure of constructing such an equivalent problem can be visualized as inserting the cylinder of interest inside an inverted cylinder (i.e. a cylindrical hole), as shown in Fig. 4. The union of these two elastic objects is an infinite elastic body. Let $\overline{\mathbf{u}}_c$ and $\overline{\mathbf{u}}_h$ be the displacement field on the surface (S) of the cylinder (C) and the hole (H), respectively; and let $\hat{\mathbf{T}}_c$ and $-\hat{\mathbf{T}}_h$ be the traction force on the surface of the cylinder and the hole, respectively. There are two different scenarios that are useful to consider separately.

First, imagine that both the cylinder and the hole have an identical displacement field at the cylindrical surface, $\overline{\mathbf{u}}_c = \overline{\mathbf{u}}_h$, as shown in Fig. 4. Let us further assume that the imposed displacement field consists of a single Fourier mode, i.e. its θ and z dependence is of the form $e^{in\theta + ik_z z}$. In this case, $\overline{\mathbf{u}}_c$ and $\hat{\mathbf{T}}_c$ are related through matrices $\mathbf{M}$ and $\mathbf{N}$, according to Eqs. (15)–(16), while $\overline{\mathbf{u}}_h$ and $\hat{\mathbf{T}}_h$ are related through matrices $\mathbf{M}'$ and $\mathbf{N}'$, according

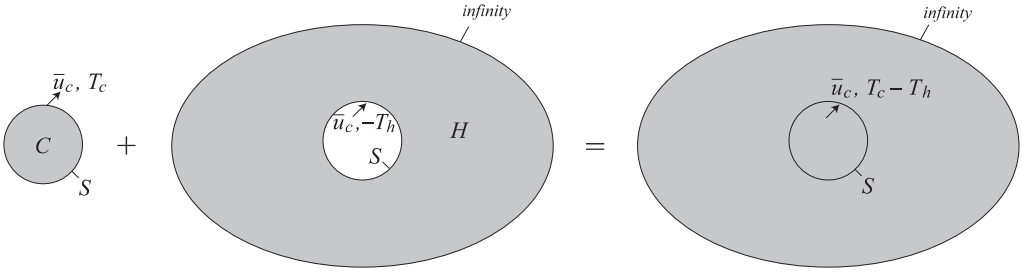

Fig. 4. Insert a cylinder into an infinite medium with a cylindrical hole with matching displacement field at the cylindrical surface, i.e. $\bar{\mathbf{u}}_c = \bar{\mathbf{u}}_h$. After the insertion, a total force of $\hat{\mathbf{T}}_c - \hat{\mathbf{T}}_h$ has to be applied at the (internal) cylindrical surface of the infinite medium to maintain equilibrium.

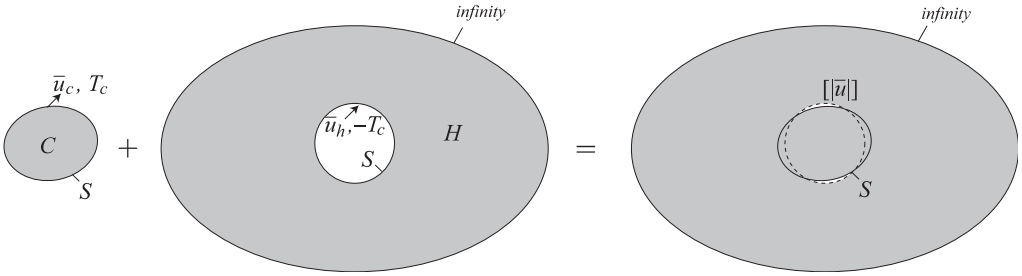

Fig. 5. Insert a cylinder into a cylindrical hole when the traction forces applied on their surfaces are equal in magnitude and opposite in direction, $\hat{\mathbf{T}}_c = \hat{\mathbf{T}}_h$. After the insertion, no external forces need to be applied to the infinite medium (because $\hat{\mathbf{T}}_c - \hat{\mathbf{T}}_h = 0$), but there will be a displacement jump across the cylindrical interface, which can be accommodated by dislocations distributed on the cylindrical surface.

to Eqs. (22)–(23),

$$\hat{\mathbf{T}}_c = \mathbf{M}\mathbf{N}^{-1}\bar{\mathbf{u}}_c, \tag{24}$$

$$\hat{\mathbf{T}}_h = \mathbf{M}'\mathbf{N}'^{-1}\bar{\mathbf{u}}_h. \tag{25}$$

After the cylinder is inserted into the hole, the displacement field will be continuous across the cylindrical surface, i.e. the displacement jump will be zero,

$$[|\hat{\mathbf{u}}|] \equiv \bar{\mathbf{u}}_c - \bar{\mathbf{u}}_h = 0 \tag{26}$$

but we still need to apply external forces at the cylindrical surface,

$$\hat{\mathbf{f}} = \hat{\mathbf{T}}_c - \hat{\mathbf{T}}_h = (\mathbf{M}\mathbf{N}^{-1} - \mathbf{M}'\mathbf{N}'^{-1})\bar{\mathbf{u}}_c \tag{27}$$

in order to maintain equilibrium. $\hat{\mathbf{f}}$ is the equivalent body force that will generate the same stress field inside the infinite body as that in the original cylinder. Given Eq. (24), the equivalent body force can also be expressed in terms of the traction force on the original cylinder, $\hat{\mathbf{T}}_c$, as

$$\hat{\mathbf{f}} = (\mathbf{I} - \mathbf{M}'\mathbf{N}'^{-1}\mathbf{N}\mathbf{M}^{-1})\hat{\mathbf{T}}_c, \tag{28}$$

where $\mathbf{I}$ is a 3×3 identity matrix.

Second, imagine the scenario that the cylinder and the hole are subjected to surface tractions that are equal in magnitude but opposite in sign, i.e. $\hat{\mathbf{T}}_c = \hat{\mathbf{T}}_h$, as shown in Fig. 5.

In this case, we will use the following relationship between $\bar{\mathbf{u}}_c$, $\hat{\mathbf{T}}_c$, $\bar{\mathbf{u}}_h$, and $\hat{\mathbf{T}}_h$:

$$\bar{\mathbf{u}}_c = \mathbf{N}\mathbf{M}^{-1}\hat{\mathbf{T}}_c, \tag{29}$$

$$\bar{\mathbf{u}}_h = \mathbf{N}'\mathbf{M}'^{-1}\hat{\mathbf{T}}_h. \tag{30}$$

After the insertion, we do not need to apply any external forces to the infinite medium because $\hat{\mathbf{T}}_c$ and $\hat{\mathbf{T}}_h$ exactly cancel each other,

$$\hat{\mathbf{f}} = \hat{\mathbf{T}}_c - \hat{\mathbf{T}}_h = 0, \tag{31}$$

but there will be a displacement jump across the cylindrical interface,

$$[|\hat{\mathbf{u}}|] \equiv \bar{\mathbf{u}}_c - \bar{\mathbf{u}}_h = (\mathbf{N}\mathbf{M}^{-1} - \mathbf{N}'\mathbf{M}'^{-1})\hat{\mathbf{T}}_c. \tag{32}$$

The displacement jump can be accommodated by introducing appropriate dislocations at the cylindrical interface. Similar to Eq. (28), we can also express the equivalent displacement jump in terms of the displacement field on the surface of the original cylinder.

$$[|\hat{\mathbf{u}}|] = (\mathbf{I} - \mathbf{N}'\mathbf{M}'^{-1}\mathbf{M}\mathbf{N}^{-1})\,\bar{\mathbf{u}}_c. \tag{33}$$

Because the original image stress problem is specified in terms of the traction force $\hat{\mathbf{T}}_c$ on the cylinder surface, Eqs. (28) and (32) will be most useful for our purposes.

When an elastic cylinder is subjected to surface traction $\mathbf{T}_c(\theta, z)$, its surface will experience a displacement $\bar{\mathbf{u}}_c(\theta, z)$. The elastic energy stored inside the cylinder can be expressed as an integral over the cylindrical surface,

$$E_c = \frac{1}{2}\int_S \mathbf{T}_c(z,\theta)\cdot\bar{\mathbf{u}}_c(z,\theta)\,\mathrm{d}S. \tag{34}$$

However, for DD simulations, we are interested in the total elastic energy, E^{tot}, of a cylinder containing a set of dislocations but subjected to traction-free boundary conditions. For example, when the dislocations are discretized into a set of nodes (connected by segments), the forces on the node i is simply

$$\mathbf{f}_i = -\frac{\partial E^{\mathrm{tot}}}{\partial \mathbf{r}_i}, \tag{35}$$

where $\mathbf{r}_i$ is the position of node i. Because analytic expressions are available for the elastic energy of an arbitrary dislocation network in an infinite medium, E^{∞}, it is useful to decompose E^{tot} into two parts,

$$E^{\mathrm{tot}} = E^{\infty} + E^{\mathrm{img}}, \tag{36}$$

where E^{img} accounts for the difference of the elastic energy when the same set of dislocation is embedded in a cylinder and that in an infinite medium. E^{img} can be readily computed using the quantities obtained above,

$$E^{\mathrm{img}} = -\frac{1}{2}\int_S \mathbf{T}_c(z,\theta)\cdot[|\mathbf{u}|](z,\theta)\,\mathrm{d}S = -\pi r L\sum_{k_z}\sum_{n}\hat{\mathbf{T}}_c(k_z,n)\cdot[|\hat{\mathbf{u}}|](-k_z,-n), \tag{37}$$

where r, L are the radius and length of the cylinder, respectively. This equation will be derived in Appendix C.

3.5. Real-space methods for image stress calculation

The two equivalent problems in the previous section can be used to construct real-space methods to compute image stress in an elastic cylinder. They are Methods II–IV shown in Fig. 2.

In Method II, the traction force $\mathbf{T}(z,\theta)$ on the cylinder surface is first transformed to Fourier space, $\hat{\mathbf{T}}(k_z,n)$, by FFT. Using Eq. (28), $\hat{\mathbf{T}}(k_z,n)$ is then converted into an equivalent set of body forces, $\hat{\mathbf{f}}(k_z,n)$, acting on the internal cylindrical interface of an infinite medium. The body forces is transformed into the real space, $\mathbf{f}(z,\theta)$, by inverse FFT.

The displacement field inside the cylinder can be obtained from the elastic Green's function (Mura, 1991),

$$u_i(\mathbf{x}) = \int_S G_{ij}(\mathbf{x}-\mathbf{x}')f_j(\mathbf{x}')\,\mathrm{d}\mathbf{x}', \tag{38}$$

where the integral is over the cylindrical surface. The stress field can be obtained from the displacement field by taking spatial derivatives and multiplying the elastic constant C_{ijkl},

$$\sigma_{ij}(\mathbf{x}) = \int_S C_{ijkl}G_{km,l}(\mathbf{x}-\mathbf{x}')f_m(\mathbf{x}')\,\mathrm{d}\mathbf{x}'. \tag{39}$$

The Green's function has an analytic expression in an isotropic linear elastic medium,

$$G_{ij}(\mathbf{x}) = \frac{1}{16\pi\mu(1-\nu)|\mathbf{x}|}\left[(3-4\nu)\delta_{ij} + \frac{x_i x_j}{|\mathbf{x}|^2}\right], \tag{40}$$

where $\nu = \lambda/2(\lambda+\mu)$ is Poisson's ratio. In practice, the integral over the cylindrical surface is approximated by a sum over a regular mesh containing a set of point forces. This method is labeled Method II (*Green*) due to the use of Green's function.

In Method III, the Fourier representation of the traction force $\hat{\mathbf{T}}(k_z,n)$ is converted, using Eq. (32), into an equivalent displacement jump, $[|\hat{\mathbf{u}}|](k_z,n)$, on the internal cylindrical interface of an infinite medium. The displacement jump is transformed into the real space, $[|\mathbf{u}|](z,\theta)$, by inverse FFT.

The elastic displacement inside the cylinder caused by this displacement jump can be obtained from Volterra's formula,

$$u_i(\mathbf{x}) = \int_S C_{jkmn}n_n G_{ij,k}(\mathbf{x}-\mathbf{x}')[|u|]_m(\mathbf{x}')\,\mathrm{d}\mathbf{x}', \tag{41}$$

where $\mathbf{n}$ is the local normal vector of the surface S. The stress field can be obtained by taking spatial derivatives and multiplying the elastic constant,

$$\sigma_{ij}(\mathbf{x}) = \int_S C_{ijkl}C_{pqrs}n_s G_{kp,ql}(\mathbf{x}-\mathbf{x}')[|u|]_r(\mathbf{x}')\,\mathrm{d}\mathbf{x}'. \tag{42}$$

In practice, the integral over the cylindrical surface is approximated by a sum over a regular mesh containing a set of infinitesimal dislocation loops. This method is labeled Method III (*Volterra*) due to the use of Volterra's formula.

Method IV follows the same procedure as Method III until the real-space displacement jump $[|\mathbf{u}|](z,\theta)$ is obtained. Instead of approximating the $[|\mathbf{u}|](z,\theta)$ field as a set of infinitesimal dislocation loops, we can approximate it as a set of overlapping rectangular dislocation loops, as shown in Fig. 6. This structure is equivalent to a network of

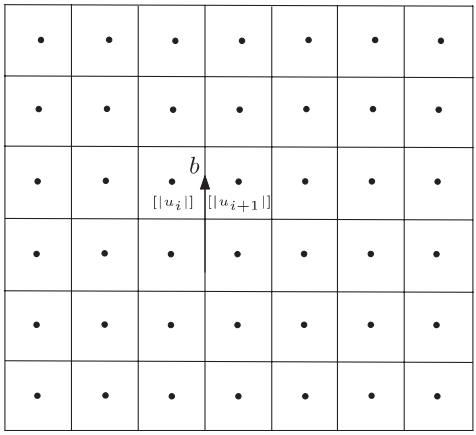

Fig. 6. The distribution of image dislocations based on displacement jump at regular sample points. The black dots represent the mesh points at which the displacement jumps are known from inverse FFT. The black lines are the dislocation line segments whose Burger's vectors are the difference between the dislocation jump at two adjacent mesh points.

dislocations, where the dislocation lines lie on the edge of the rectangles. We call these dislocations segments image dislocations, to distinguish them from the "real" dislocations that may exist inside the cylinder. The Burgers vector on each segment is the difference between the displacement jump at neighboring sample points. (It is easy to show that the Burgers vector is conserved at every node where four dislocation segments join together.) The image stress field can then be computed from these image dislocation segments using Mura's formula,

$$\sigma_{\alpha\beta}(\mathbf{x}) = \oint C_{\alpha\beta kl}\varepsilon_{lnh}C_{pqmn}b_m v_n(\mathbf{x}')G_{kp,q}(\mathbf{x}-\mathbf{x}')\,\mathrm{d}L(\mathbf{x}'). \tag{43}$$

The $\oint$ symbol emphasizes the fact that the Burgers vector must be conserved everywhere (in other words, the dislocation line cannot end by itself). Analytic expressions for the stress field produced by an arbitrary straight dislocation segment have been derived for isotropic linear elastic infinite medium (Hirth and Lothe, 1982). The stress field of the image dislocation network can then be computed as the sum of the contribution from each straight segment. This method is labeled Method IV (*Mura*) due to the use of Mura's formula.

Methods II–IV all have the advantage that, being real-space methods, they can make use of the FMM to enhance computational efficiency. The stress contributions from body forces or image dislocations far away from the field point can be lumped together and represented by a multipole expansion. The stress field produced by body forces or image dislocations are also sufficiently simple to allow analytic integrations over straight segments (that experience the Peach–Koehler force). In particular, both FMM and analytic expressions of stress integrated over straight segments have been implemented in the ParaDiS DD code. This means that, presently, Method IV has the advantage that it can use the efficient stress calculation algorithm that is already implemented in DD simulations. However, the implementation of FMM and analytic expressions of stress integrals is also straightforward for Methods II and III. We expect this to be a worthwhile

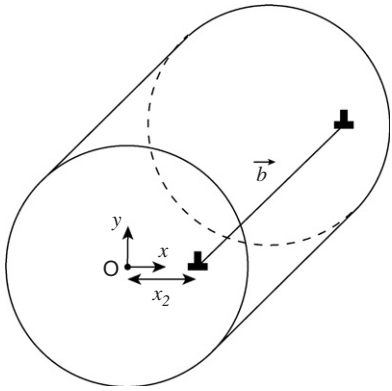

Fig. 7. An infinite straight edge dislocation in a cylinder offset by x_2.

endeavor because Methods II and III seem to have better convergence behavior than Method IV, as will be seen in Section 4.

Because PBC are applied along the z axis, we need to account for the stress contributions from an infinite number of replicas of each point force or image dislocation on the cylindrical interface. This can be easily done within the FMM (Challacombe et al., 1997).

Recently, a non-singular continuum theory of dislocations has been developed where the difficulty of defining self-forces on dislocations has been removed by allowing dislocations to spread out smoothly in space (Cai et al., 2006). The advantages of this theory can be inherited in Method IV since we have converted the original problem to an infinite elastic medium containing a set of "real" and "image" dislocations. The same idea can also be applied to Methods II and III to remove the elastic singularity self-consistently.

4. Numerical results

In this section, we present three test cases to check the convergence, accuracy, and self-consistency of all the methods presented above, i.e. I (*Bessel*), II (*Green*), III (*Volterra*), IV (*Mura*), for computing image stresses and image forces on dislocations in a cylinder.

4.1. Test case 1

Consider, for numerical comparison, the image stress of a straight edge dislocation inside a cylinder. As shown in Fig. 7, the Burgers vector is along x and the dislocation is offset from the origin along x by x_2. The image stress field of this configuration has been found analytically[2] (Eshelby, 1979). The stress component that gives rise to a Peach–Koehler force on the dislocation itself is

$$\sigma_{xy}^{\text{img}} = \frac{\mu b x_2}{2\pi(1-\nu)(r^2 - x_2^2)}. \tag{44}$$

[2]Eshelby also obtained the analytic expressions for the screw dislocation of a similar configuration, which could be used for comparison as well.

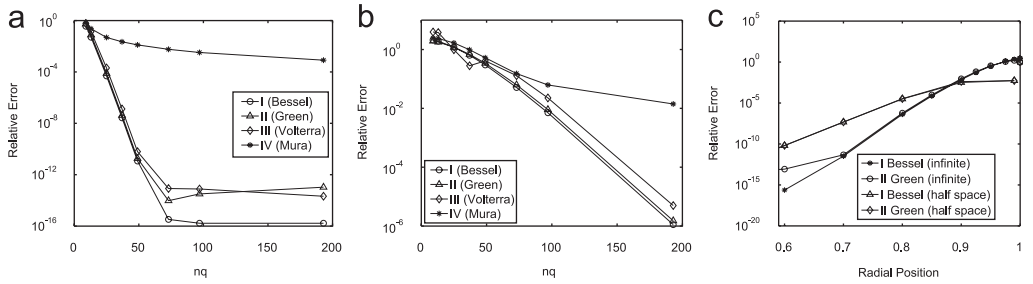

Fig. 8. The relative error as a function of the number of grid points in the perimeter, n_q, for the image force on an edge dislocation located at (a) $x_2 = 0.5$ and (b) $x_2 = 0.9$. (c) The relative error as a function of radial position for the infinite body and half space solutions.

This will be used as a benchmark to compare with our numerical results. For simplicity, we choose the parameters such that $\mu b/2\pi(1-\nu) = 1$, the cylinder radius $r = 1$ and length $L = 6$. Fig. 8(a) and (b) shows the relative error of the four numerical methods as a function of n_q for the cases of $x_2 = 0.5$ and 0.9, respectively. The number of mesh points along the cylinder axis is kept at $n_z = 2n_q$. For Methods II–IV, the effect of periodic images along the cylindrical axis (where PBC is applied) is accounted for by including 50 images on each side explicitly, and using a multipole expansion for the rest.

In Fig. 8(a), Methods I–III all show exponential decay of the relative error with increasing n_q (as indicated by a straight line in the semi-log plot), until round-off precision is reached. However, Method IV (using finite image dislocation segments) shows a much slower, power-law convergence.

Fig. 8(b) shows that the convergence is slower for all methods when the field point (now B) moves closer to the cylindrical surface. In particular, Method III (*Volterra*) shows very large error for at low n_q. This is because the stress field of an infinitesimal dislocation loop scales as $\mathcal{O}(R^{-3})$, where R is the distance between the field point and the image dislocation loop (on the cylindrical surface). In comparison, the stress field of a point force and that of an infinitesimal dislocation segment both scale as $\mathcal{O}(R^{-2})$. Therefore, Method II (*Green*) and IV (*Mura*) both show a higher accuracy at point B compared with Method III (*Volterra*). Nonetheless, at sufficiently large n_q, all methods exhibit good numerical accuracy compared with analytic solutions. These results suggest that it may be advantageous to use different methods to compute image stress depending on the distance between the field point and the cylindrical surface. For example, Methods II–IV all suffer from singularities of stress sources at the cylinder surface. However, the solution from Method I contains no singularities and is completely well behaved.

Fig. 8(a) and (b) indicates that, for a fixed number of surface mesh points, the accuracy of our numerical results deteriorates as the dislocation approaches the cylindrical surface. In Methods II–IV, the image stress fields are represented by the superposition of the singular stress fields of equivalent stress sources (body forces, displacement jumps, or image dislocations). When the separation between the dislocation and the free surface is smaller than the distance between neighboring mesh points, the dislocation will experience the singularity of these equivalent stress sources and the numerical error is expected to be large. Fig. 8(c) plots the relative error of the image stress as a function of the dislocation position for both Methods I and II with $n_q = n_z/2 = 97$. Two sets of data are shown, corresponding to two different approaches to obtain the image stress. The first approach is

the same as that used in Fig. 8(a) and (b) where numerical method is directly applied to compute the image stress. The relative error exceeds 50% when x_2 reaches 95% of the cylinder radius. The second approach takes advantage of the analytic solution for the dislocation stress field in an elastic half space. The numerical method only computes the difference between the image stress for the dislocation in an elastic cylinder and that in the half space (see Section 2). The surface of the elastic half space is chosen to be tangent to the cylindrical surface at the intersection with the positive x axis. The relative error in the second approach is smaller than 0.5% regardless of the dislocation position. This is because the image stress solution in an elastic half space becomes an increasingly better approximation for the image stress in a cylinder as the dislocation approaches the cylindrical surface. It is also interesting that the relative error for Method I and Method II are comparable in both approaches, even though Method I is free from the artificial singularities that exist in Method II. This suggests that the "singularity amplification" is not a main source of numerical error in the image stress calculation here. In practical applications, it is advisable to take advantage of the analytic solutions of dislocation stress fields in an elastic half space, which also exist in 3D (Gosling and Willis, 1994), to reduce numerical error. This idea has been discussed in Tang et al. (2006) and can be combined with the methods presented in this paper.

4.2. Test case 2

The test case considered above is a 2-dimensional problem which only tests the special case of $k_z = 0$ for our algorithms. In this test case, we consider a circular prismatic dislocation loop concentric with the cylindrical axis, discretized with 10 equally spaced nodes connected by straight segments, as shown in Fig. 9(a). The radius of the cylinder is

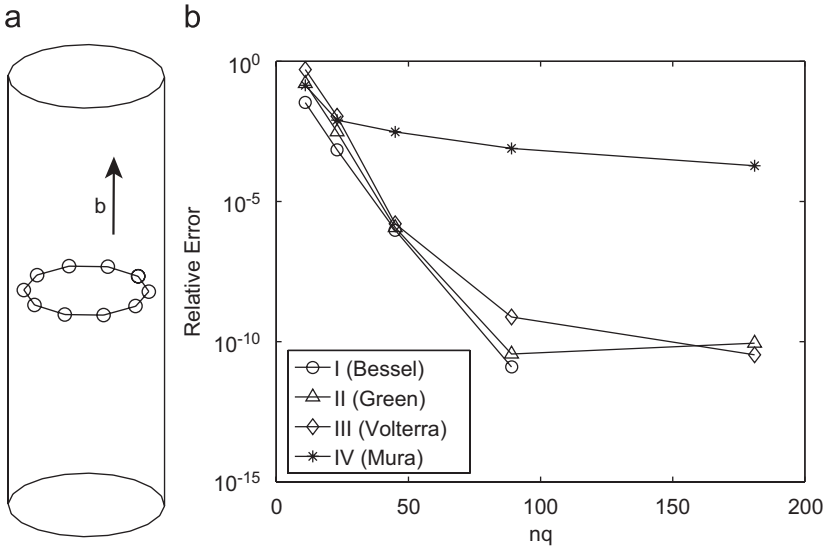

Fig. 9. (a) A concentric prismatic loop in a cylinder. (b) The relative error in the image force acting on the node as a function of n_q.

$r = 1$ and the length is $L = 6$. The radius of the dislocation loop is $r_d = 0.8$. The Burgers vector is parallel to the cylinder axis and has magnitude 1.

In Methods I–III, the image forces on the dislocation nodes are calculated by numerically integrating the stress field on neighboring segments using the midpoint rule with 10 quadrature points. In Method IV (*Mura*), because the image stress fields are represented in terms of image dislocation segments, the image nodal forces are computed using the analytic expressions for the stress field of one segment integrated over another segment (Cai et al., 2004; Arsenlis et al., 2007). In Methods II–IV, the effects of the periodic images (along z-axis) are incorporated by explicitly calculating the effect of 10 images (above and below) and using a multipole expansion for the rest. Due to the symmetry of this problem, the image forces on all nodes point to the radial direction and have the same magnitude. An estimate of their relative error is plotted as a function of n_q in Fig. 9. Because this problem does not have an analytic solution, the reference value is taken to be the value obtained using Method I (*Bessel*) with $n_q = 181$. At around $n_q = 50$, the relative error of all methods becomes lower than 1%.

4.3. Test case 3

Test case 1 only covers plane strain applications while test case 2 approximates a concentric circular prismatic loop that, with a infinitesimal discretization, would be axisymmetric. Thus, for this test case we consider the more general case of the image forces on a glide dislocation loop. The cylindrical axis is along the [1 1 0] axis of a cubic crystal, and the dislocation loop lies on its glide plane which is (1 1 1). The Burgers vector is along $[\bar{1}\,1\,0]$ (perpendicular to the cylinder axis) and has magnitude 1. The dislocation loop is discretized by 10 equally spaced nodes connected by straight segments. The orientation

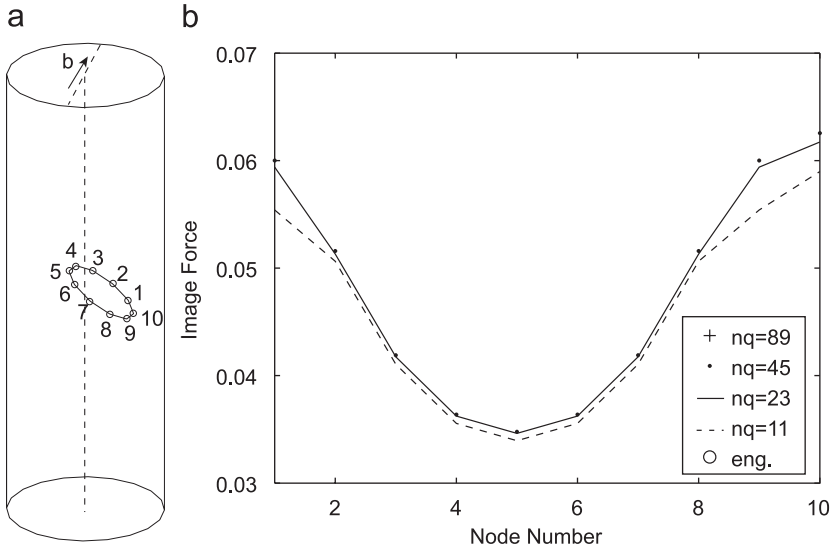

Fig. 10. (a) An off-center tilted glide loop in a cylinder. (b) The magnitude of the image force on each node of the glide loop resolved on the glide plane.

and magnitude of the image force on every node is different. Fig. 10 plots the component of the image force in the direction away from the center of the loop for all 10 nodes with different values of n_q using Method IV (*Mura*).

The convergence of the image force with respect to n_q is faster for nodes closer to the center of the cylinder than that for the nodes closer to the cylinder surface. We also computed the image elastic energy of the configuration using Eq. (37). The image forces on the nodes can then be computed by displacing the nodal positions in small steps and numerically differentiating the image elastic energy. The image forces computed in this way with $n_q = 45$ are plotted as circles in Fig. 10(b), which agrees with the values obtained by integrating the image stress field along the dislocation segment. This confirms the self-consistent nature of our theory and the numerical algorithm.

5. Discussion

Speed and accuracy are important aspects of an image stress method when applied to DD simulations because the stress field needs to be computed at every time step of a DD simulation. Here we discuss the speed, accuracy and scaling behavior of the methods developed here and compare them with the finite element method (FEM) and the boundary element method (BEM).

There are obvious parallels between the algorithms developed here, particularly Method III (Green), and BEM. Similar to BEM, our methods require a 2-dimensional mesh on the cylindrical surface, on which the traction force $\mathbf{T}$ is sampled. In both Method III and BEM, these surface tractions are then converted to a set of body forces in an infinite medium, distributed over the same mesh. However, our methods perform the conversion faster than BEM. Let $N = n_q \times n_z$ be the total number of mesh points on the cylindrical surface. The standard BEM requires an inversion of a dense $N \times N$ matrix, which requires $\mathcal{O}(N^2)$ operations. In Methods I–IV, we take advantage of the fact that the elasticity equations are decoupled in Fourier space. The most time-consuming part of the conversion is the FFT, which requires $\mathcal{O}(N \ln N)$ operations. The conversion from surface traction to body force in the Fourier space only requires the inversion of N 3×3 matrices, which requires $\mathcal{O}(N)$ operations.

After the distribution of body forces (or image dislocations) are obtained, the calculation of the image stress inside the cylinder is essentially the same for BEM and for the methods described here. Let N_d be the number of dislocation segments inside the cylinder (on which the image stress field needs to be computed). The total number of operations for image stress calculation can be kept at $\mathcal{O}(N + N_d)$ if fast multipole method (FMM) is used.

The methods developed here may be faster than FEM if the same level of accuracy for the stress field is demanded for both methods. The stress field for Methods I–III converges to analytic results exponentially, while power-law convergence is expected for FEM. Because the FEM mesh is 3-dimensional, the total number of mesh points should be $N_{FEM} \propto N^{3/2}$, assuming a uniform mesh with aspect ratio of each element close to 1. Therefore, the computational cost for FEM should be at least $\mathcal{O}(N_{FEM}) = \mathcal{O}(N^{3/2})$ (Cook et al., 2001). When the cylinder contains only a few dislocation segments, i.e. in the limit of $N_d \ll N$, our methods should be faster than FEM. In the limit of $N_d \gg N$, $N_d = \mathcal{O}(N_{FEM})$ our methods and FEM should scale similarly.

Another advantage of our methods (and BEM) is that, once the stress sources are converted to a set of body forces (or image dislocations) in an infinite medium, the stress integral over another straight segment is available analytically. The analytic expressions for the stress integrals have been used in DD simulations in the bulk and are found to significantly increase the computational efficiency. This should further increase the efficiency of image force calculations in our methods.

An advantage of the standard BEM and FEM methods is that, at least in principle, the surface can be remeshed if necessary. This allows the use of a non-uniform mesh, e.g. a denser mesh where a dislocation intersects the surface and a coarser mesh elsewhere. This also allows the possibility to resolve the surface step created by the dislocations that exit the surface. In comparison, this is not possible in our methods, because they rely on the translational and rotational symmetry of the elastic cylinder. However, the effect of the surface step can be approximated, to the first order, by a line force on the surface. This solution can be superimposed on the solution developed here. On the other hand, representing small surface steps explicitly in FEM or BEM is usually not a good idea, because it requires a very dense mesh near the surface step, which will raise the computational cost significantly. This makes the line force approximation a more appealing alternative when the cylinder is not excessively deformed. If the crystal becomes highly distorted, as in the late stages of deformation, this approximation will no longer be appropriate. When this happens, we will have to use the standard FEM or BEM method, but the medium must be continually remeshed, which will raise the computational cost of FEM and BEM as well.

6. Conclusions

We have developed a method to compute the stress field inside an elastic cylinder subjected to arbitrary traction force on the surface. The resulting driving force on the dislocations inside the cylinder can be computed efficiently by transforming the problem into a set of image dislocations in an infinite elastic medium. The transformation can be done efficiently by FFT and a set of analytic expressions. This allows efficient calculation of the effect of free surface on the driving force of dislocation segments, using the computer programs already developed for bulk DD simulations.

Acknowledgments

The authors wish to thank Profs. C.R. Steele, D.M. Barnett, W.D. Nix, and P. Pinsky for useful discussions. The work is partly supported by an NSF Career Grant CMS-0547681. C.R. Weinberger is supported by a Benchmark Stanford Graduate Fellowship.

Appendix A. The infinite cylinder solution

Here we give the analytic expressions for the matrices **M** and **N** introduced in Section 3.2 and discuss their special cases. The **M** and **N** matrices are a simple way to relate the Fourier components of the tractions and displacements in cylindrical coordinates on the surface to the unknown coefficients A, B, and C. These matrices also play an important role in finding the equivalent problems in an infinite medium. For the Fourier mode that

varies with z (i.e. $k_z \neq 0$), the nine components of $\mathbf{M}$ and $\mathbf{N}$ are

$$
\begin{aligned}
M_{11} &= \frac{2\mu}{\lambda+2\mu}\{\mathrm{i}J_{n+1}(\mathrm{i}k_z)[(\lambda+2\mu)k_z(n+1)+(\lambda+\mu)(k_z^3+n^2k_z)] \\
&\quad + J_n(\mathrm{i}k_z)(\lambda+\mu)(k_z^2-k_z^2n+n^2-n^3)\}, \\
M_{12} &= 2\mu k_z[\mathrm{i}(n+1)J_n(\mathrm{i}k_z)+k_zJ_n(k_z)], \\
M_{13} &= 2\mu n[\mathrm{i}k_zJ_n(\mathrm{i}k_z)+J_n(\mathrm{i}k_z)(1-n)], \\
M_{21} &= -\frac{\mu}{\lambda+2\mu}\{J_{n+1}(\mathrm{i}k_z)[\mu(-4k_z-6k_zn)+\lambda(-2k_z-4k_zn)] \\
&\quad + \mathrm{i}J_n(\mathrm{i}k_z)[\mu(-2n^2+2k_z^2n+2k_z^2+2n^3)+\lambda(2k_z^2n-2n^2+k_z^2+2n^3)]\}, \\
M_{22} &= \mu k_z[2J_{n+1}(\mathrm{i}k_z)(n+1)-\mathrm{i}k_zJ_n(\mathrm{i}k_z)], \\
M_{23} &= \mu[2k_zJ_{n+1}(\mathrm{i}k_z)+\mathrm{i}J_n(\mathrm{i}k_z)(2n-2n^2-k_z^2)], \\
M_{31} &= -\frac{\mathrm{i}\mu k_z}{\lambda+2\mu}J_n(\mathrm{i}k_z)(2k_z^2\lambda+n\lambda+2\mu k_z^2+2\lambda n^2+2\mu n+2\mu n^2), \\
M_{32} &= \mu k_z[2k_zJ_{n+1}(\mathrm{i}k_z)+\mathrm{i}nJ_n(\mathrm{i}k_z)], \\
M_{33} &= -\mathrm{i}\mu n k_zJ_n(\mathrm{i}k_z)
\end{aligned}
\tag{A.1}
$$

and

$$
\begin{aligned}
N_{11} &= -\frac{1}{\lambda+2\mu}[J_n(\mathrm{i}k_z)(\lambda+\mu)(k_z^2+n^2)+\mathrm{i}k_zJ_{n+1}(\mathrm{i}k_z)(2\mu+\lambda)], \\
N_{12} &= -\mathrm{i}k_zJ_{n+1}(\mathrm{i}k_z), \\
N_{13} &= -nJ_n(\mathrm{i}k_z), \\
N_{21} &= -\frac{1}{\lambda+2\mu}\{J_{n+1}(\mathrm{i}k_z)[(\lambda+\mu)nk_z+(\lambda+2\mu)k_z]+\mathrm{i}n^2J_n(\mathrm{i}k_z)(\lambda+\mu)\}, \\
N_{22} &= -k_zJ_{n+1}(\mathrm{i}k_z), \\
N_{23} &= -k_zJ_{n+1}(\mathrm{i}k_z)-\mathrm{i}nJ_n(\mathrm{i}k_z), \\
N_{31} &= -\frac{k_z}{\lambda+2\mu}\{k_zJ_{n+1}(\mathrm{i}k_z)(\lambda+\mu)+\mathrm{i}J_n(\mathrm{i}k_z)[(\lambda+2\mu)+n(\lambda+\mu)]\}, \\
N_{32} &= \mathrm{i}k_zJ_n(\mathrm{i}k_z), \\
N_{33} &= 0.
\end{aligned}
\tag{A.2}
$$

The above expressions are only valid when $k_z \neq 0$. When $k_z = 0$, the displacement potential must be rewritten in terms of powers of r. For the solution to be bounded at $r = 0$, different displacement potentials must be used for $n>0$, $n<0$ and $n = 0$. For $n>0$ the

displacement potential is

$$\begin{aligned}
\phi &= \frac{\mu}{\lambda+2\mu} A r^{n+2} \mathrm{e}^{\mathrm{i}n\theta}, \\
\psi_r &= -\mathrm{i}B r^{n+1} \mathrm{e}^{\mathrm{i}n\theta}, \\
\psi_\theta &= B r^{n+1} \mathrm{e}^{\mathrm{i}n\theta}, \\
\psi_z &= [C r^n + \mathrm{i}A r^{n+2}] \mathrm{e}^{\mathrm{i}n\theta}
\end{aligned} \tag{A.3}$$

and the **M** and **N** matrices are

$$\mathbf{M} = \begin{bmatrix}
-\dfrac{2\mu}{\lambda+2\mu}(\mu+\lambda)(n^2-n-2) & 0 & 2\mathrm{i}(n-1)\, n\mu \\
-\dfrac{2\mathrm{i}\mu}{\lambda+2\mu} n(n+1)(\mu+\lambda) & 0 & -2(n-1)\, n\mu \\
0 & 2\mu n & 0
\end{bmatrix}, \tag{A.4}$$

$$\mathbf{N} = \begin{bmatrix}
-\dfrac{n(\lambda+\mu)-2\mu}{\lambda+2\mu} & 0 & \mathrm{i}n \\
-\mathrm{i}\dfrac{n(\lambda+\mu)+2(\lambda+2\mu)}{\lambda+2\mu} & 0 & -n \\
0 & 2 & 0
\end{bmatrix}. \tag{A.5}$$

For the case when $n<0$ the displacement potential is

$$\begin{aligned}
\phi &= \frac{\mu}{\lambda+2\mu} A r^{-n+2} \mathrm{e}^{\mathrm{i}n\theta}, \\
\psi_r &= \mathrm{i}B r^{-n+1} \mathrm{e}^{\mathrm{i}n\theta}, \\
\psi_\theta &= B r^{-n+1} \mathrm{e}^{\mathrm{i}n\theta}, \\
\psi_z &= [C r^{-n} - \mathrm{i}A r^{-n+2}] \mathrm{e}^{\mathrm{i}n\theta}
\end{aligned} \tag{A.6}$$

and the **M** and **N** matrices are

$$\mathbf{M} = \begin{bmatrix}
-\dfrac{2\mu}{\lambda+2\mu}(\mu+\lambda)(n^2+n-2) & 0 & -2\mathrm{i}(n+1)n\mu \\
\dfrac{2\mathrm{i}\mu}{\lambda+2\mu} n(n-1)(\mu+\lambda) & 0 & -2(n+1)n\mu \\
0 & -2\mu n & 0
\end{bmatrix}, \tag{A.7}$$

$$\mathbf{N} = \begin{bmatrix}
\dfrac{n(\lambda+\mu)+2\mu}{\lambda+2\mu} & 0 & \mathrm{i}n \\
-\mathrm{i}\dfrac{n(\lambda+\mu)-2(\lambda+2\mu)}{\lambda+2\mu} & 0 & n \\
0 & 2 & 0
\end{bmatrix}. \tag{A.8}$$

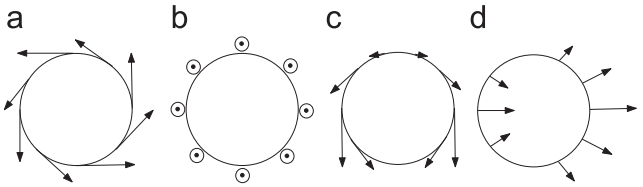

Fig. 11. Modes of traction forces (with $k_z = 0$) that cannot be supported by the cylinder. (a) Net torque associated with T_θ, (b) net force in the z-direction associated with T_z, (c) and (d) net forces in the x- and y-directions associated with both T_θ and T_r.

For $n = 0$ and $k_z = 0$, the displacement potential is

$$\phi = Ar^2,$$
$$\psi_\theta = Br,$$
$$\psi_z = Cr^2 \tag{A.9}$$

and the **M** and **N** matrices become

$$\mathbf{M} = \begin{bmatrix} 4(\lambda+\mu) & 0 & 0 \\ 0 & 0 & 0 \\ 0 & 0 & 0 \end{bmatrix}, \tag{A.10}$$

$$\mathbf{N} = \begin{bmatrix} 2 & 0 & 0 \\ 0 & 0 & 2 \\ 0 & 2 & 0 \end{bmatrix}. \tag{A.11}$$

The cases where $k_z = 0$ and $n = -1, 0$ or 1 the **M** matrices are singular. This corresponds to the inability of the cylinder to support a net force or a net torque. For example, a non-zero $\hat{T}_\theta$ for the Fourier mode $k_z = 0$ and $n = 0$ leads to a net torque around z-axis, and a non-zero $\hat{T}_z$ for the same Fourier mode leads to a net force along z-axis, as shown in Fig. 11(a) and (b).The other two net loads correspond to forces in the x- and y-directions when $k_z = 0$ and $n = \pm 1$, as shown in Fig. 11(c) and (d). The inverse of **M** can be obtained from the psuedo-inverse defined through the singular value decomposition (Strang, 2005).

Appendix B. The infinite cylindrical hole solution

The solution to the inverted cylinder problem (infinite hole) relies on the matrices $\mathbf{M}'$ and $\mathbf{N}'$, which are analogous to the **M** and **N** matrices for the cylinder problem. When the solution varies with z (i.e. $k_z \neq 0$), the $\mathbf{M}'$ and $\mathbf{N}'$ have the same form as **M** and **N** given in Appendix A for the cylinder problem, except J_n is replaced by the Hankel functions of the first or second kind, H_n^α. The choice of the Hankel function depends on the sign of k_z, H_n^1 for positive k_z and H_n^2 for negative k_z. Similarly, the $\mathbf{M}'$ matrices become singular in some special cases.

If the solution does not depend on z, then the solution must be in powers of r and plane waves in θ. This solution must again be divided into cases where $n < 0$ and $n > 0$ so that the solution is bounded as $r \to \infty$.

The displacement potential for $n>0$ is

$$\begin{aligned}
\phi &= \frac{\mu}{\lambda+2\mu} A r^{-n+2} \mathrm{e}^{\mathrm{i}n\theta}, \\
\psi_r &= \mathrm{i}B r^{-n+1} \mathrm{e}^{\mathrm{i}n\theta}, \\
\psi_\theta &= B r^{-n+1} \mathrm{e}^{\mathrm{i}n\theta}, \\
\psi_z &= [C r^{-n} - \mathrm{i}A r^{-n+2}] \mathrm{e}^{\mathrm{i}n\theta}
\end{aligned} \tag{B.1}$$

and the $\mathbf{M}'$ and $\mathbf{N}'$ matrices are

$$\mathbf{M}' = \begin{bmatrix} -\dfrac{2\mu}{\lambda+2\mu}(\mu+\lambda)(n^2+n-2) & 0 & -2\mathrm{i}(n+1)\,n\mu \\ \dfrac{2\mathrm{i}\mu}{\lambda+2\mu} n(n-1)(\mu+\lambda) & 0 & -2(n+1)\,n\mu \\ 0 & -2\mu n & 0 \end{bmatrix}, \tag{B.2}$$

$$\mathbf{N}' = \begin{bmatrix} \dfrac{n(\lambda+\mu)+2\mu}{\lambda+2\mu} & 0 & \mathrm{i}n \\ -\mathrm{i}\dfrac{n(\lambda+\mu)-2(\lambda+2\mu)}{\lambda+2\mu} & 0 & n \\ 0 & 2 & 0 \end{bmatrix}. \tag{B.3}$$

The $n<0$ potential and associated $\mathbf{M}'$ and $\mathbf{N}'$ matrices are

$$\begin{aligned}
\phi &= \frac{\mu}{\lambda+2\mu} A r^{n+2} \mathrm{e}^{\mathrm{i}n\theta}, \\
\psi_r &= -\mathrm{i}B r^{n+1} \mathrm{e}^{\mathrm{i}n\theta}, \\
\psi_\theta &= B r^{n+1} \mathrm{e}^{\mathrm{i}n\theta}, \\
\psi_z &= [C r^{n} + \mathrm{i}A r^{n+2}] \mathrm{e}^{\mathrm{i}n\theta}
\end{aligned} \tag{B.4}$$

and

$$\mathbf{M}' = \begin{bmatrix} -\dfrac{2\mu}{\lambda+2\mu}(\mu+\lambda)(n^2-n-2) & 0 & 2\mathrm{i}(n-1)n\mu \\ -\dfrac{2\mathrm{i}\mu}{\lambda+2\mu} n(n+1)(\mu+\lambda) & 0 & -2(n-1)n\mu \\ 0 & 2\mu n & 0 \end{bmatrix}, \tag{B.5}$$

$$\mathbf{N}' = \begin{bmatrix} -\dfrac{n(\lambda+\mu)-2\mu}{\lambda+2\mu} & 0 & \mathrm{i}n \\ -\mathrm{i}\dfrac{n(\lambda+\mu)+2(\lambda+2\mu)}{\lambda+2\mu} & 0 & -n \\ 0 & 2 & 0 \end{bmatrix}. \tag{B.6}$$

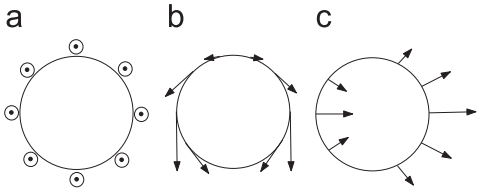

Fig. 12. Modes of traction forces (with $k_z = 0$) that cannot be supported by an infinite medium with a cylindrical hole. (a) Net force in the z-direction associated with T_z, (b) and (c) net forces in the x- and y-directions associated with both T_θ and T_r.

For the $k_z = 0$ and $n = 0$ case the potential is

$$\begin{aligned} \phi &= A\ln(r), \\ \psi_\theta &= Br, \\ \psi_z &= C\ln(r) \end{aligned} \tag{B.7}$$

and the $\mathbf{M}'$ and $\mathbf{N}'$ matrices are

$$\mathbf{M}' = \begin{bmatrix} -2\mu & 0 & 0 \\ 0 & 0 & 2\mu \\ 0 & 0 & 0 \end{bmatrix}, \tag{B.8}$$

$$\mathbf{N}' = \begin{bmatrix} 1 & 0 & 0 \\ 0 & 0 & -1 \\ 0 & 2 & 0 \end{bmatrix}. \tag{B.9}$$

The cylindrical hole solution also has problems with net applied loads. The solution will not support net applied forces in the x-, y- and z-directions as shown in Fig. 12.However, it will support a net torque, which is related to the fact that the rank of the matrix $\mathbf{M}'$ is 2 when $n = 0$ and $k_z = 0$ (whereas the rank of $\mathbf{M}$ is 1 when $n = 0$ and $k_z = 0$).

Appendix C. Image energy

Here we derive the expression for the image energy, Eq. (37). According to Eq. (36), E^{img} is defined as the difference between the total elastic energy of an elastic cylinder containing a set of dislocations (system 1) and the elastic energy of an infinite medium containing the same set of dislocations (system 2), i.e.

$$E^{\text{img}} = E^{\text{tot}} - E^{\infty}. \tag{C.1}$$

Let σ_{ij}^{∞} and e_{ij}^{∞} be the stress and elastic strain field of the dislocations in an infinite medium. Let σ_{ij}^{tot} and e_{ij}^{tot} be the stress and elastic strain field of the same dislocations in the elastic cylinder. Then the image stress and elastic fields can be defined as

$$\begin{aligned} \sigma_{ij}^{\text{img}} &= \sigma_{ij}^{\text{tot}} - \sigma_{ij}^{\infty}, \\ e_{ij}^{\text{img}} &= e_{ij}^{\text{tot}} - e_{ij}^{\infty}. \end{aligned} \tag{C.2}$$

Therefore,

$$E^{\infty} = \frac{1}{2}\int_{\infty} \sigma_{ij}^{\infty} e_{ij}^{\infty}\, \mathrm{d}V,$$
$$E^{\mathrm{tot}} = \frac{1}{2}\int_{\Omega} (\sigma_{ij}^{\infty} + \sigma_{ij}^{\mathrm{img}})(e_{ij}^{\infty} + e_{ij}^{\mathrm{img}})\, \mathrm{d}V. \tag{C.3}$$

The first integral is over the infinite medium and the second integral is over the volume of the cylinder. The variation of E^{tot} gives rise to two Peach Koehler forces, the self-force of a dislocation in an infinite medium plus the image force. A good discussion of this and full proof can be found in Gavazza and Barnett (1975). In principle, E^{img} can be derived by taking the difference between the above two equations. However, it is more convenient to consider a reversible path that can convert system 2 (E^{∞}) to system 1 (E^{tot}). If the work done by the external force along this path is ΔW, then

$$E^{\mathrm{img}} = \Delta W. \tag{C.4}$$

Let us consider a path shown in Fig. 13.The first step is to cut a cylindrical region out of the infinite medium, while maintaining a traction force $\mathbf{F}$ on the surface of the cylinder and $-\mathbf{F}$ on the cylindrical hole, where $F_j = \sigma_{ij}^{\infty} n_i^{\mathrm{out}}$. n_i^{out} is the outward normal of the cylindrical surface. This will ensure that the stress field and the elastic energy do not change. The second step is to reduce the traction forces on both surfaces to zero. Inside the cylinder, this is equivalent to superimposing the image solution, corresponds to a defect-free elastic cylinder subject to traction forces $T_j = -F_j$ on its surface, as in Section 2. Let $\mathbf{u}_{\mathrm{c}}$ be the displacement on the cylindrical surface when a defect-free cylinder is subjected to surface traction $\mathbf{T}$. Let $\mathbf{u}_{\mathrm{h}}$ be the displacement on the cylindrical surface when a defect-free infinite medium with a cylindrical hole is subjected to traction force $-\mathbf{T}$ on its inner surface. Then

$$\begin{aligned} E^{\mathrm{img}} = \Delta W &= \int_S \frac{1}{2}(\mathbf{F})\cdot(\mathbf{u}_{\mathrm{c}}) + \frac{1}{2}(-\mathbf{F})\cdot(\mathbf{u}_{\mathrm{h}})\, \mathrm{d}S \\ &= -\frac{1}{2}\int \mathbf{T}\cdot(\mathbf{u}_{\mathrm{c}} - \mathbf{u}_{\mathrm{h}})\, \mathrm{d}S \\ &= -\frac{1}{2}\int \mathbf{T}\cdot[|\mathbf{u}|]\, \mathrm{d}S. \end{aligned} \tag{C.5}$$

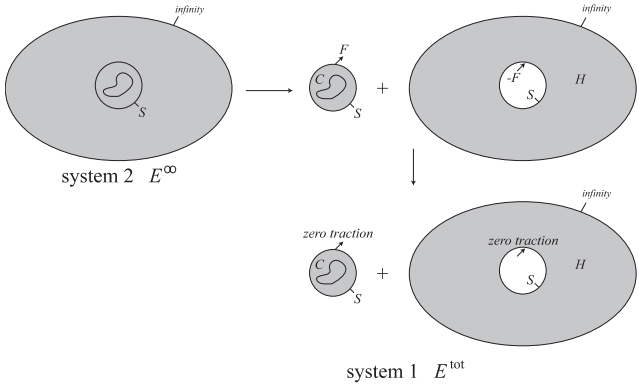

Fig. 13. A reversible path to convert an infinite medium containing a set of dislocations (system 2) to an elastic cylinder containing the same set of dislocations (system 1).

Computing the image energy allows us to check the self-consistency in the image force calculation. Consider a dislocation discretizied by straight segments connecting a set of nodes. The total force $\mathbf{f}_i^{\text{tot}}$ on node i can be computed by integrating the total stress field over its neighboring segments (with appropriate weighting functions) and using the Peach–Koehler formula. For self-consistency, the total force and total energy must satisfy the following relationship:

$$\mathbf{f}_i^{\text{tot}} = -\frac{\partial E^{\text{tot}}}{\partial \mathbf{r}_i}. \tag{C.6}$$

Similarly, the image force $\mathbf{f}_i^{\text{tot}}$ on node i can be computed by integrating the image stress field over its neighboring segments and using the Peach–Koehler formula. For self-consistency, the image force and total energy must satisfy

$$\mathbf{f}_i^{\text{img}} = -\frac{\partial E^{\text{img}}}{\partial \mathbf{r}_i}. \tag{C.7}$$

This is verified numerically in Section 4.4. The total force can be expressed by a sum

$$\mathbf{f}_i^{\text{tot}} = \mathbf{f}_i^{\infty} + \mathbf{f}_i^{\text{img}}, \tag{C.8}$$

where

$$\mathbf{f}_i^{\infty} = -\frac{\partial E^{\infty}}{\partial \mathbf{r}_i} \tag{C.9}$$

is the force on node i if the same dislocation resides in an infinite medium. The self-consistency required by Eq. (C.9) in an infinite medium was discussed in Cai et al. (2006).

References

Achenbach, J.D., 1982. Wave Propagation in Elastic Solids. North-Holland, Amsterdam.

Arsenlis, A., Cai, W., Bulatov, V.V., Rhee, M., Tang, M., Oppelstrup, T., Hiratani, M., Hommes, G., Pierce, T.G., 2007. Enabling strain hardening simulations with dislocation dynamics, submitted to MSMSE.

Bulatov, V.V., Cai, W., Fier, J., Hiratani, M., Pierce, T., Tang, M., Rhee, M., Yates, K., Arsenlis. A., 2004. Scalable line dynamics in ParaDiS Supercomputing, 19.

Cai, W., Bulatov, V.V., Pierce, T.G., Hiratami, M., Rhee, M., Bartelt, M., Tang, M., 2004. Massively-Parallel Dislocation Dynamics Simulations. In: Solid Mechanics and Its Applications, vol. 115, Kluwer Academic Publishers, Dordrecth, p. 1.

Cai, W., Arsenlis, A., Weinberger, C.R., Bulatov, V.V., 2006. A non-singular continuum theory of dislocations. J. Mech. Phys. Solids 54, 561–587.

Challacombe, M., White, C., Head-Gordon, M., 1997. Periodic boundary conditions and the fast multipole method J. Chem. Phys. 107, 10131–10140.

Chau, K.T., Wei, X.X., 2000. Finite solid circular cylinders subjected to arbitrary surface load. Part I—analytic solution. Int. J. Solids Struct. 37, 5707–5732.

Chree, C., 1889. The equations of an isotropic elastic solid in polar and cylindrical co-ordinates, their solution and application. Cambridge Philos. Trans. 14, 250–369.

Cook, R.D., Malkus, D.S., Plesha, M.E., Witt, R.J., 2001. Concepts and Applications of Finite Element Analysis, fourth ed. Wiley, New York.

Devincre, B., Kubin, L.P., 1997. Mesoscopic simulations of dislocations and plasticity. Mater. Sci. Eng. 234–236, 8–14.

Eshelby, J.D., 1979. Boundary problems. In: Nabarro, F.R.N. (Ed.), Dislocations in Solids, vol. 1. North-Holland, Amsterdam, p. 167.

Gavazza, S.D., Barnett, D.M., 1975. Image force on a dislocation loop in a bounded elastic medium. Scr. Metall. 9, 1263–1265.

Ghoniem, N.M., Han, X., 2005. Dislocation motion in anisotropic multilayer materials. Philos. Mag. 85, 2809–2830.
Ghoniem, N.M., Sun, L.Z., 1999. Fast-sum method for the elastic field off three-dimensional dislocation ensembles. Phys. Rev. B 60, 128–140.
Gosling, T.J., Willis, J.R., 1994. Line-integral representation for the stresses due to an arbitrary dislocation in an isotropic half-space. J. Mech. Phys. Solids 42, 1199–1221.
Greer, J.R., Nix, W.D., 2006. Nanoscale gold pillars strengthened through dislocation starvation. Phys. Rev. B 73, 245410.
Greer, J.R., Oliver, W.C., Nix, W.D., 2005. Size dependence of mechanical properties of gold at the micron scale in the absence of strain gradients. Acta Mater. 52, 1821–1830.
Hirth, J.P., Lothe, J., 1982. Theory of Dislocations. Wiley, New York.
Kim, Y.Y., Steele, C.R., 1989a. End effects and time-harmonic longitudinal wave propagation in a semi-infinite solid cylinder. J. Appl. Mech. 56, 334–346.
Kim, Y.Y., Steele, C.R., 1989b. Effects of lateral surface conditions in time-harmonic nonsymmetric wave propagation in a cylinder. J. Appl. Mech. 56, 910–917.
Kim, Y.Y., Steele, C.R., 1990. Analytic-asymptotic approach for time-harmonic nonsymmetric wave propagation in a cylinder. Int. J. Solid. Struct. 26, 1143–1157.
Kim, Y.Y., Steele, C.R., 1992. Static axisymmetric end problems in semi-infinite and finite solid cylinders. J. Appl. Mech. 57, 69–76.
Lubarda, V.A., 1999. On the non-uniqueness of solution for screw dislocations in multiply connected regions. J. Elasticity 52, 289–292, (1998–1999).
Mura, T., 1991. Micromechanics of Defects in Solids, second rev. ed. Kluwer Academic Publishers, Dordrecht.
Nicola, L., Xiang, Y., Vlassak, J.J., Van der Giessen, E., Needleman, A., 2006. Plastic deformation of freestanding thin films: Experiments and modeling. J. Mech. Phys. Solids 54, 2089–2110.
Nix, W.D., Greer, J.R., Feng, G., 2004. A dislocation multiplication length scale for plasticity: strain hardening in small crystals by dislocation starvation. J. Met. 56, 36–37.
Pochammer, L., 1876. Beitrag zur theorie der biegung des Kreiscylinders. Crelles J. 81, 33.
Schwarz, K.W., 1999. Simulation of dislocations on the mesoscopic scale. I. Methods and examples. J. Appl. Phys. 85, 108–119.
Schwarz, K.W., 2003. Discrete dislocation dynamics study of strained-layer relaxation. Phys. Rev. Lett. 91, 145503.
Strang, G., 2005. Linear Algebra and Its Applications. Brooks Cole.
Swadener, J.G., George, E.P., Pharr, G.M., 2002. The correlation of the indentation size effect measured with indenters of various shapes. J. Mech. Phys. Solids 50, 681–694.
Tang, M., Cai, W., Xu, G., Bulatov, V.V., 2006. A hybrid method for computing forces on curved dislocations intersecting free surfaces in three-dimensional dislocation dynamics. Modelling Simul. Mater. Sci. Eng. 14, 1139–1151.
Uchic, M.D., Dimiduk, D.M., Florando, J.N., Nix, W.D., 2004. Sample dimensions influence strength and crystal plasticity. Science 305, 986–989.
Uchic, M.D., Dimiduk, D.M., Wheeler, R., Shade, P.A., Fraser, H.L., 2006. Applications of micro-sample testing to study fundamental aspects of plastic flow. Scr. Mater. 54, 759–764.
Wei, X.X., Chau, K.T., 2000. Finite solid circular cylinders subjected to arbitrary surface load. Part II—application to double-punch test. Int. J. Solid. Struct. 37, 5733–5744.
Weygand, D., Friedman, L.H., Van der Giessen, E., Needleman, A., 2001. Discrete dislocation modeling in three-dimensional confined volumes. Mater. Sci. Eng. A 309–310, 420–424.
Weygand, D., Friedman, L.H., Van der Giessen, E., Needleman, A., 2002. Aspects of boundary-value problem solutions with three-dimensional dislocation dynamics. Model. Simul. Mater. Sci. Eng. 10, 437–468.
Wu, B., Heidelberg, A., Boland, J.J., 2005. Mechanical properties of ultrahigh-strength gold nanowires. Nat. Mater. 4, 525–529.
Zuo, L., Ngan, A.H.W., 2006. Molecular dynamics study on compressive yield strength in Ni_3Al micro-pillars. Philos. Mag. Lett. 86, 355–365.